An S-scheme CeO$_2$/ foveolate g-C$_3$N$_4$ composite with horseradish peroxidase activity for photo-enzyme synergistic catalytic degradation of phenanthrene

Chujun Feng [a], Jian Rong [b], Yuzhe Zhang [b], Xudong Zheng [b], Xiazhang Li [c], Song Xu [c,*], Zhongyu Li [a,b,c,**]

[a] School of Safety Science and Engineering, Changzhou University, Changzhou 213164, PR China
[b] School of Environmental Science and Engineering, Changzhou University, Changzhou 213164, PR China
[c] Jiangsu Key Laboratory of Advanced Catalytic Materials and Technology, School of Petrochemical Engineering, Changzhou University, Changzhou 213164, PR China

ARTICLE INFO

ABSTRACT

Nanozyme technology is a relatively new technology that has shown promising applications in the removal of water pollutants. This study utilized a CeO$_2$/foveolate g-C$_3$N$_4$ (CeO$_2$/FCN) composite with S-scheme heterojunction to achieve efficient removal of Phenanthrene (PHE) through a combination of photocatalytic and enzymatic reactions. The S-scheme heterojunction was effective in inhibiting the recombination of photo-generated electron hole pairs, which promoted the generation of·OH and·O$_2$. Additionally, activated H$_2$O$_2$ enables Ce to achieve redox cycle reaction and generate more·OH for catalytic degradation, effectively improving the concentration of active species and promoting the photo-enzyme synergistic catalytic performance. The experimental results showed that PHE degradation efficiency of CeO$_2$/FCN composite could reach 96.6% in 60 min. Furthermore, the photo-enzyme synergistic catalytic mechanism of CeO$_2$/FCN composite and the possible intermediates generated in the degradation process were studied. The highly toxic PHE was converted into non-toxic green degradation products, providing an effective method for the photo-enzyme synergistic catalytic degradation of PAHs.

1. Introduction

Polycyclic aromatic hydrocarbons (PAHs) are a group of organic compounds containing two or more fused aromatic rings, such as benzene, naphthalene, and Phenanthrene [1]. They are usually released by incomplete combustion of fossil fuels, wood, tobacco, and organic polymers. PAHs, as well as their oxidized derivatives, are known to be highly toxic, teratogenic, and carcinogenic to humans, animals, and plants [2,3]. Phenanthrene (PHE) is a low molecular weight PAH with a very stable three-ring structure, which makes it durable and difficult to degrade [4,5]. Therefore, it is of great significance to find a green and efficient degradation technology to remove PHE.

Enzyme catalysis technology has shown infinite possibilities in solving the problem of water pollutants due to its characteristics of high selectivity, gentleness, strong specificity and adjustable activity [6–8]. Compared with natural enzymes, Nanozyme not only inherit the enzymatic activity, but also have better adaptability to the environment and show good stability [9–11]. Cerium dioxide (CeO$_2$) has a highly reversible Ce^{3+}/Ce^{4+} redox pair, which exhibits a variety of enzymatic activities, including horseradish peroxidase (HRP) [12–14]. HRP uses hydrogen peroxide as a substrate to catalyze the oxidation of various materials, which is widely used in food science and environmental remediation [14]. However, Nanozyme itself showed limited enzymatic activity and could not achieve efficient degradation of water pollutants. According to the research of predecessors, nano-enzyme materials as one of the products of nanomaterial development, which possess both the physical and chemical properties of nanomaterials, including optical properties. The optical properties can be used to enhance the photocatalytic activity of nanomaterials. Therefore, by combining enzyme catalysis with photocatalysis, the problem of low pollutant removal efficiency can be effectively solved, and the nano-enzyme material can become a dual-function material [15,16].

At present, photocatalysis technology is regarded as a promising technology for pollutants degradation [17–22]. Highly active species generated in the photocatalysis process, such as superoxide radical ($\cdot O_2^-$) and hydroxyl radical ($\cdot OH$), could oxidize large organic pollutants into small molecular compounds and eventually completely mineralize into H_2O and CO_2 [23–27]. As a two-dimensional conjugated polymer semiconductor, graphite-phase carbon nitride (g-C_3N_4) has the advantages of good redox capacity, adjustable band gap, environmental protection and pollution-free in the photocatalysis process [7]. However, it is inevitable that the specific surface area of g-C_3N_4 is relatively low and the recombination rate of photogenerated electron hole pairs is relatively high, which is not conducive to the formation of more highly active groups [6]. To address this issue, the S-scheme heterojunction has received a lot of attention recently. S-scheme heterojunction can usually solve the problem that a single semiconductor material cannot realize the efficient separation of photogenerated electrons. When there are staggered energy bands and appropriate Fermi energy levels (E_f) between two semiconductors, the difference in their EF levels creates a potential gradient at their interface, which leads to the flow of electrons from the high EF side to the low EF side until they reach equilibrium. This flow of electrons generates an internal electric field (IEF) at their interface, which is accompanied by band bending. The IEF between them accelerates the transfer of photogenerated charge carriers, and the curved band acts as a check valve to control the transfer direction of photogenerated electrons and holes, which can realize the spatial separation of charge carriers and maintain a strong redox capacity [28,29].

In this work, we propose a photo-enzyme synergistic catalytic strategy for band structure engineering and morphology engineering of foveolate CeO₂/FCN composite, with PHE as a simulated pollution to achieve high efficiency degradation performance. The S-scheme heterojunction not only has the excellent charge separation performance to continuously provides effective energy for the entire reaction, but also retains strong redox ability. Coupled with the HRP activity to increase the amount of active group generation, the catalytic performance of S-scheme CeO₂/FCN composite is significantly improved. The experimental results showed that CeO₂/FCN composite showed good photo-enzyme synergistic catalytic performance under different conditions. At the same time, the possible degradation products and mechanism of photo-enzyme synergistic catalysis was deduced, and it was found that H_2O_2 is not the only terminal oxidant for HRP initiation, and some $\cdot OH$ can also be produced in the photocatalytic process. In addition, h^+ and $\cdot O_2^-$ generated during photocatalysis also contribute to the catalytic degradation of PHE. The photo-enzyme synergistic catalytic strategy provides a reasonable and effective method for the improvement of enzyme catalytic activity and the efficient separation of photogenerated electron-hole pairs, and provides a potential way for the development of the degradation of PAHs pollutants.

2. Experimental section

2.1. Preparation of foveolate g-C₃N₄ (FCN)

The foveolate g-C_3N_4 (FCN) was prepared by a facile thermal copolymerization method [30]. The process began with the dispersion of 1.0 g melamine and 1.5 g cyanuric acid in 30 mL and 20 mL of dimethyl sulfoxide, forming two solutions A and B. Solution B was then added drop by drop to solution A and stirred vigorously for 2 h. After stirring, 100 mL H_2O was added to the mixture and leave overnight to form a white precipitate. The white precursor was obtained by centrifugation and drying. Finally, the white precursor was transferred to a tubular furnace and calcined at 550 °C for 4 h at a heating rate of 2 °C/min. After calcination, the foveolate g-C_3N_4 (FCN) is obtained by grinding.

2.2. Preparation of CeO₂

CeO₂ was prepared according to previous methods [31]. Initially,

1.0 g Ce(NO₃)₃ was weighed and added to 30 mL H_2O, resulting in solution C after stirring for 30 min. Next, 8.0 g NaOH was dissolved in 10 mL H_2O to obtain solution D. Solution D was then added to solution C and kept at 200 °C for 24 h. After cooling to room temperature, white samples were obtained by centrifugal drying. Finally, the CeO₂ nanoparticles were calcined at 350 °C for 4 h in a tubular furnace.

2.3. Preparation of CeO₂/FCN composite

CeO₂/FCN composite was synthesized mainly by ultrasonic impregnation (Scheme 1). Initially, 0.5 g FCN and x% CeO₂ were added to 15 mL ethanol and dispersed under ultrasonic conditions for 1 h, resulting in E solution and F solution. Next, F solution was added drop by drop to E solution, and ultrasound was continued for 30 min. After ultrasound, 15 mL acetone was added, and the mixture was stirred overnight. Finally, the CeO₂/FCN composite was obtained by centrifugation and drying.

2.4. Characterization

The crystal structure and chemical structure of the prepared samples were analyzed by XRD and XPS. The morphology of the prepared samples was analyzed by SEM, and the microstructure was further determined by TEM and HRTEM. The specific surface area, pore volume and pore size distribution of the prepared samples were determined by N₂ adsorption-desorption analyzer (ASAP2020PLUS). The Zeta potential of the sample was determined by Zeta potential analyzer (ZetaView PMX120). The electrochemical characterization was performed on an electrochemical workstation (CHI760E).

2.5. Peroxidase-like activity measurements

The peroxidase activity of the prepared samples was evaluated by using chromogenic peroxidase probes (TMB). First, 20 μL of MTB-DMSO solution (1 mM) and 200 μL of the prepared sample-NaAc solution (150 μg/mL) were absorbed. After mixing them well, 80 μL of H_2O_2 solution (1 mM) is added to it. Then the mixture is placed in a dark place for 10 min to allow the peroxidase activity to occur. The absorbance at 652 nm associated with Ox TMB was measured with an ultraviolet spectrophotometer at the end of the standing.

2.6. Photo-enzyme synergistic degradation of phenanthrene (PHE)

The photo-enzyme synergistic catalytic performance of CeO₂/FCN composites was evaluated by PHE solution at 5 mg/L. Specifically, 0.02 g of different catalysts were dispersed in 50 mL PHE solution. Then it was transferred to the photocatalytic reaction instrument and tested with 1000 W mercury lamp as the simulated light source. During the test, the reaction solution (3 mL) was sucked by pipette every 10 min and filtered with 0.22 μm syringe filter. The concentration of PHE was determined by measuring the absorbance at 293 nm with an ultraviolet spectrophotometer.

3. Results and discussion

3.1. Chemical composition and microstructure

The crystal structure and phase of the photocatalyst were analyzed by X-ray diffraction (XRD). As shown in Fig. 1, FCN has two distinct diffraction peaks at around 13.1° and 27.3°, corresponding to the (100) and (002) crystal planes respectively. These peaks are attributed to the interlayer superposition of the aromatic system and triazine repeating units. The diffraction peaks near 28.5°, 33.0°, 47.4°, 56.3°, 59.0°, 69.4°, 76.6°, and 79.0° matched the crystal planes (111), (200), (220), (311), (222), (400), (331) and (420) in the CeO₂ standard card (PDF#34–0394), indicating that CeO₂ has a high crystallinity. The
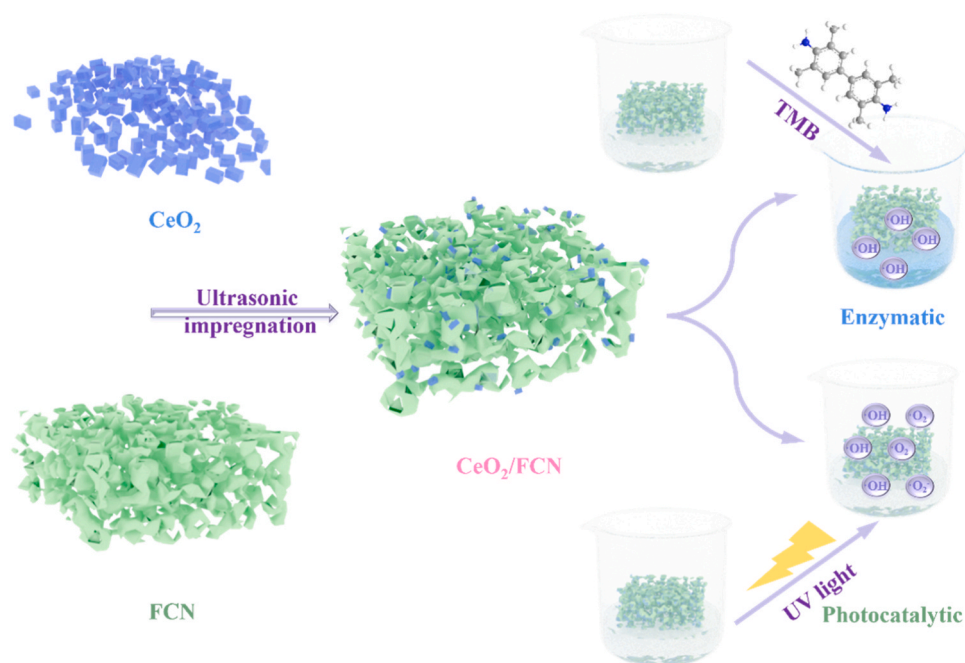
Scheme 1. Schematic diagram for the preparation of CeO$_2$/FCN composite.
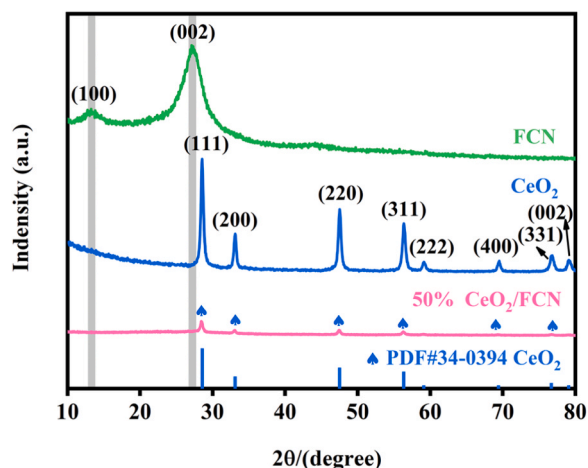

Fig. 1. XRD pattern of the prepared catalysts.

characteristic peak of CeO$_2$ can be observed on CeO$_2$/FCN, but the characteristic peak of FCN is not obvious, which may be caused by the high peak intensity of CeO$_2$.

The chemical state of the composite was detected by X-ray photoelectron spectroscopy (XPS). In Fig. 2a, CeO$_2$/FCN composite can clearly observe the characteristic peaks related to C, N, Ce and O. As shown in Fig. 2b, the C-C characteristic peak at 284.80 eV is considered to be the amorphous carbon deposition on the photocatalyst surface. The two peaks at 286.49 eV and 288.34 eV were assigned to C-O and C=O of FCN. The N 1 s spectrum of CeO$_2$/FCN composite can be convolved into three characteristic peaks with binding energies of 398.63 eV, 398.18 eV and 400.45 eV, which are attributed to are attributed to N = N-C, tertiary nitrogen (N-(C)$_3$) groups and C-NH$_2$ groups, respectively (Fig. 2c). It can be seen from Fig. 2d that Ce element mainly exists in a mixed valence state of Ce^{3+} and Ce^{4+}. For CeO$_2$, Ce 3d is convolved into eight characteristic peaks, where μ and v represent the Ce 3d$_{5/2}$ and Ce 3d$_{3/2}$ spin orbits of Ce ion, respectively. Among them, v$_1$ (916.56 eV), v$_2$ (907.45 eV), v$_4$ (900.89 eV), μ$_1$ (898.21 eV), μ$_2$ (888.72 eV) and μ$_4$ (882.39 eV) can be attributed to Ce^{4+}, while the locations of v$_3$

(903.09 eV) and μ$_3$ (884.41 eV) can be attributed to Ce^{3+}. Obviously, Ce 3d binding energy of CeO$_2$/FCN composite is significantly higher than that of CeO$_2$. A similar phenomenon can be observed in O 1 s, and the binding energy of M-O (528.68 eV) and O-H (531.17 eV) in the CeO$_2$ is lower than that of CeO$_2$/FCN composite (Fig. 2e). On the contrary, the binding energy of the characteristic peaks of C 1 s and N 1 s in the FCN increased slightly. In general, the binding energy of constituent elements increases or decreases correspondingly when electron loss or gain occurs, this change trend reveals strong interactions between CeO$_2$ and FCN, which contributes to the formation of heterojunction.

The morphology of the as-prepared composite was studied by scanning electron microscope (SEM). It can be seen that FCN formed a loose multi-layer foveolate structure (Fig. 3a), while CeO$_2$ mainly presented a nanoparticle structure (Fig. 3b). As shown in Fig. 3(c, d), the CeO$_2$ particles with regular morphology are uniformly deposited on the surface of FCN, and the CeO$_2$/FCN composite maintains the original concave structure of FCN. At the same time, it can be found from Fig. 3e that all elements are uniformly distributed on the CeO$_2$/FCN composite, indicating the successful loading of CeO$_2$ and FCN. The microstructure of the photocatalyst was confirmed by transmission electron microscopy (TEM). The TEM images reveal that FCN is a foveolate material composed of multi-layer porous structures (Fig. 3(f, j)), while CeO$_2$ is mainly a crystal particle with a random size distribution between 15 nm and 50 nm (Fig. 3g). In the corresponding HRTEM images (Fig. 3(h, i)), the (111) crystal plane of CeO$_2$ with the lattice spacing of 0.313 nm can be clearly observed. In the TEM image of the CeO$_2$/FCN composite (Fig. 3k), CeO$_2$ is uniformly dispersed on the surface of FCN, and there is an obvious close contact at the interface between CeO$_2$ and FCN. The interfacial interaction between CeO$_2$ and FCN was further analyzed by HRTEM, and the lattice fringe corresponding to CeO$_2$ (111) crystal plane was obviously observed (Fig. 3(l, m)). These results indicate that there is a close interfacial contact between CeO$_2$ and FCN in the CeO$_2$/FCN composite, which is important for understanding the photocatalytic properties of the composite.

Subsequently, the specific surface area and pore volume of FCN, CeO$_2$ and CeO$_2$/FCN composite were tested by N$_2$ adsorption-desorption experiment. It can be clearly observed that the prepared samples display type IV isotherms with type H3 hysteresis loop, indicating that samples have the mesoporous structure which has been confirmed by aperture
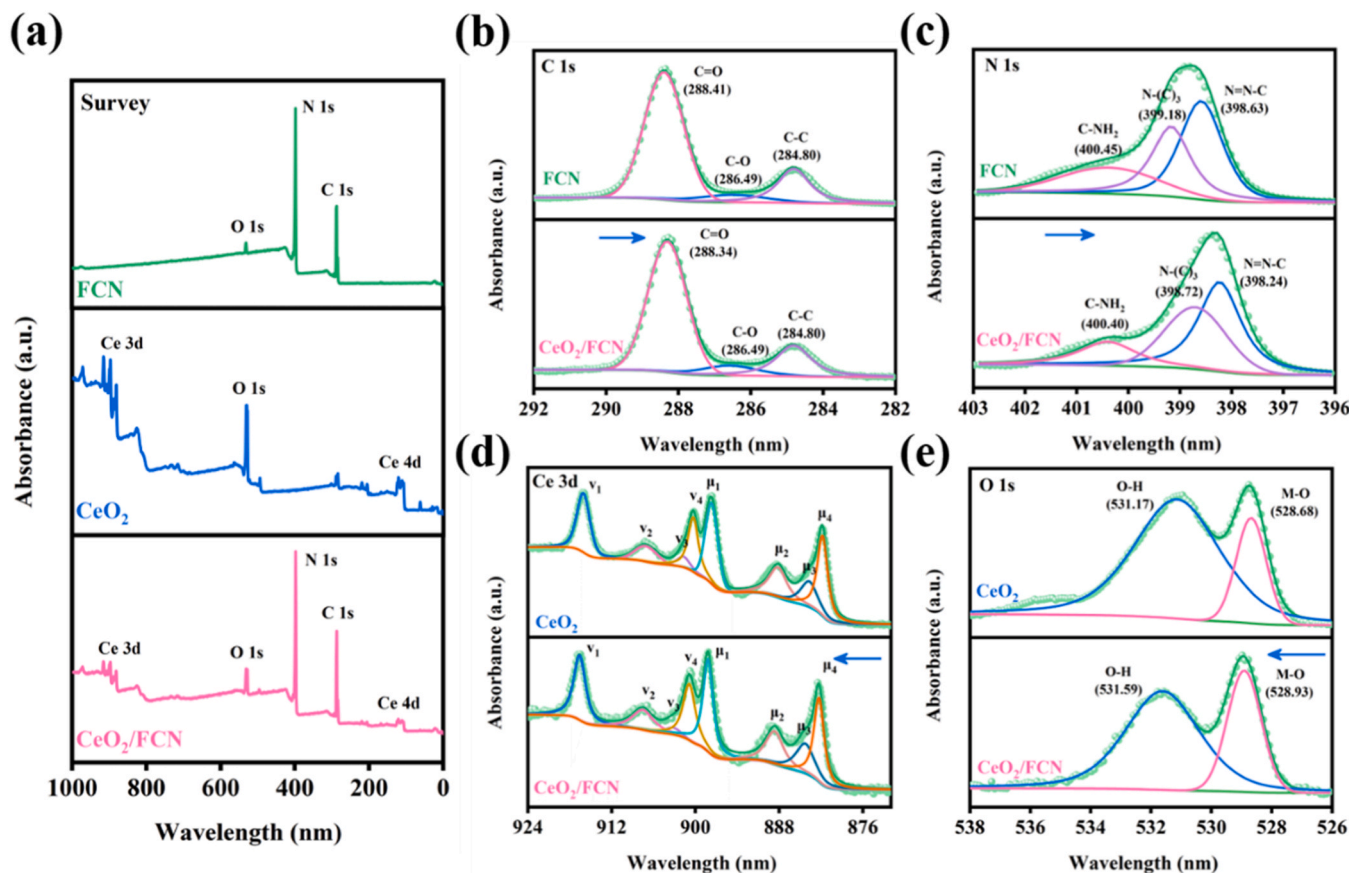
Fig. 2. XPS spectra of FCN, CeO_2 and CeO_2/FCN composite: (a) full-range scan of the prepared catalysts and High-resolution XPS spectrum of (b) C 1 s, (c) N 1 s, (d) Ce 3d and (e) O 1 s.

distribution diagram (Fig. S1) [6,32]. The specific surface area of FCN from BET analysis is 81.3039 m^2/g, while the specific surface area of CeO2/FCN composite obtained by combining with CeO_2 (28.4653 m^2/g) is 54.8914 m^2/g (Table S1). Compared with FCN, the specific surface area decreased slightly, which may be due to the partial collapse of FCN pores due to the introduction of CeO_2 [33].

3.2. Peroxidase-like activity of CeO_2/FCN composite

According to previous studies, the dynamic and reversible changes between Ce^{4+} and Ce^{3+} give the nanoparticles horseradish peroxidase (HRP) activity [13,34]. In order to verify whether CeO_2/FCN composite has horseradish peroxidase properties, 3, 3′, 5, 5′-tetramethylbenzidine (TMB) was used as the model substrate for enzymatic oxidation, and the results are shown in Fig. 4. The chromogenic changes of TMB, FCN, CeO_2 and CeO_2/FCN composite were simulated in the presence of H_2O_2. It is not difficult to find that CeO_2 and CeO_2/FCN composite produce maximum absorption at 652 nm (Fig. 4a), and the solution changes from colorless to dark blue due to the CeO_2/FCN composite catalyzed TMB to produce Ox TMB (Fig. 4b) [7,16]. Therefore, it is suggested that CeO_2/FCN composite has horseradish peroxidase properties. In addition, the enzymatic chromogenic reaction of CeO_2/FCN composite under light conditions was simulated. Under light conditions, CeO_2/FCN composite still showed horseradish peroxidase properties, and the solution color was relatively darker, showing better enzymatic reaction results (Fig. 4c). This may be because CeO_2/FCN composite also generate·OH from h^+ under light conditions, effectively increasing the concentration of·OH [7,35]. It is proved that CeO_2/FCN composite can achieve photo-enzyme system catalytic degradation reaction.

3.3. Photo-enzyme synergistic catalytic performance

The photo-enzyme synergistic catalytic activity of CeO_2/FCN composite is related to its ability to degrade PHE solution (5 mg/L, pH=7) under UV light. In Fig. 5a, the degradation efficiency of PHE in the presence of only H_2O_2 was first tested. There is no significant degradation of PHE can be observed under the condition of only H_2O_2, so the degradation performance of H_2O_2 can be ignored. Subsequently, the photo-enzyme synergistic catalytic effect under different catalysts was tested, and it was found that the photo-enzyme catalytic effect of x% CeO_2/FCN composites was significantly higher than that of pure FCN or CeO_2. Meanwhile, when the mass fraction of CeO_2 was 50%, the photo-enzyme synergistic catalytic activity was the best about 96.6%. When CeO_2 mass fraction was 70%, the catalytic performance began to decline. On the one hand, excessive addition of CeO_2 might increase the turbidity and affect the transmittance; On the other hand, an excess amount of CeO_2 can reduce the separation efficiency of charge carriers, which can ultimately lead to a decrease in the photocatalytic activity (Fig. 7c). In addition, the mechanically mixed sample is denoted as FCN+CeO_2 mixed, and its photo-enzyme synergistic catalytic activity is significantly lower than 50% CeO_2/FCN, which verifies that the strong interfacial interaction between FCN and CeO_2 helps to improve the photo-enzyme synergistic catalytic performance. The catalytic performance of other studied catalysts for degradation of PHE is listed in Table S2. The results showed that 50% CeO_2/FCN composite was able to degrade high concentration PHE solution with relatively less catalyst amount and relatively short degradation time, indicating its potential as an efficient photo-enzyme catalyst for environmental remediation. Fig. 5b shows that the photo-enzyme synergistic catalytic degradation rate of the prepared catalysts conforms to the first-order kinetic
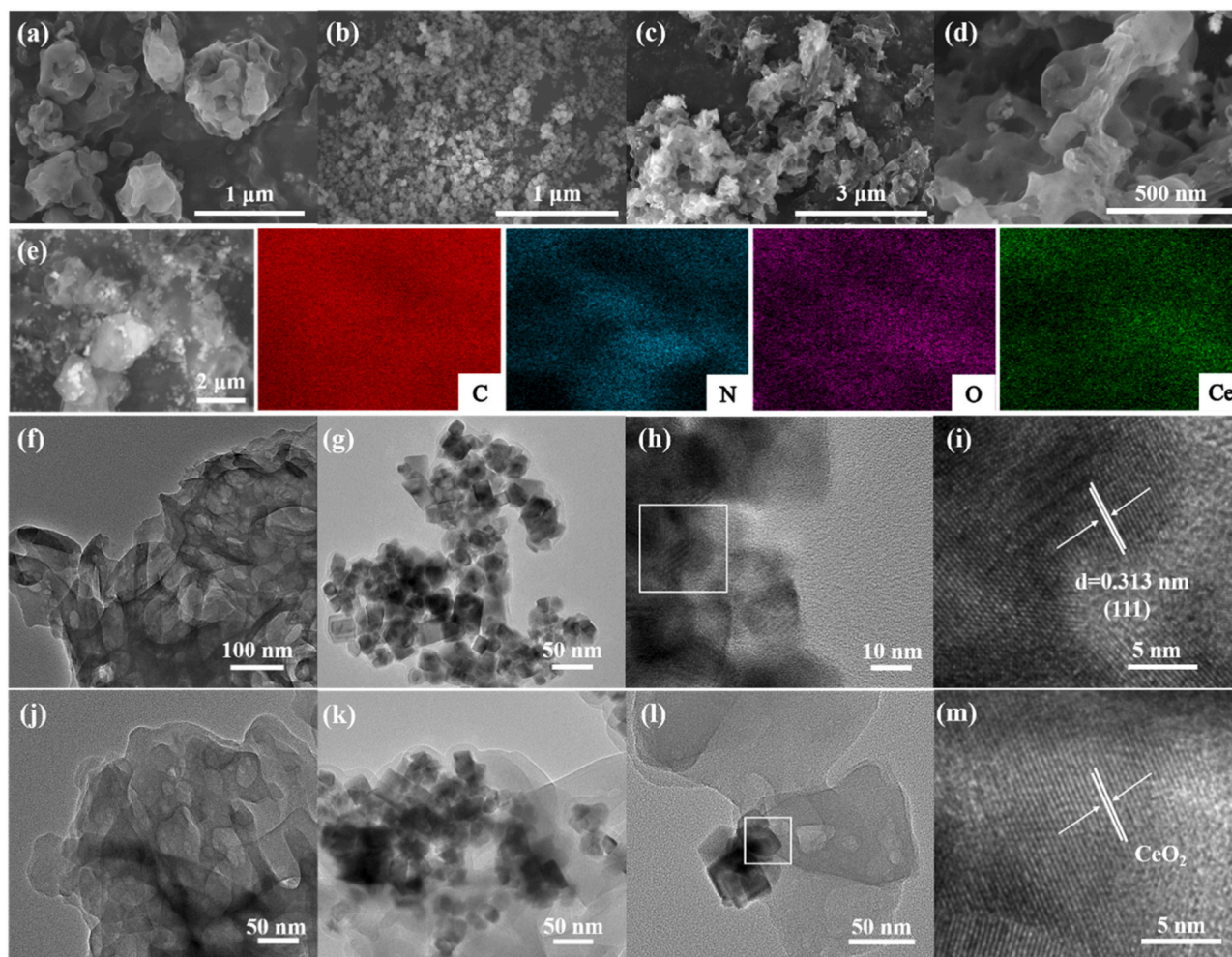
Fig. 3. SEM image of (a) FCN, (b) CeO₂, (c, d) the CeO₂/FCN composite and (e) the elemental mapping of the CeO₂/FCN composite; TEM image of (f, j) FCN; (g, h) TEM and (i) HRTEM image of CeO₂; (k, l) TEM and (m) HRTEM image of the CeO₂/FCN composite.
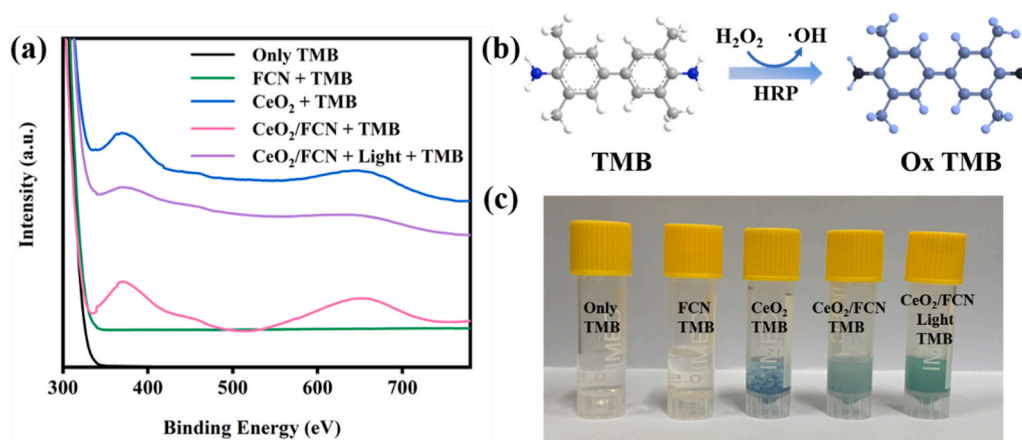
Fig. 4. UV–vis absorbance spectra of the catalytic activity of HRP on TMB of different catalysts under different conditions; (b) Oxidation equation for TMB and (c) Chromogenic changes of TMB oxidized by different catalysts.

equation. The maximum degradation rate of 50% CeO₂/FCN is about $0.05436 \ min^{-1}$, and its degradation rate was about 7.05 times and 6.05 times than that of FCN ($0.00771 \ min^{-1}$) and CeO₂ ($0.00899 \ min^{-1}$). In addition, the synergy factor of the photo-enzyme synergistic system of CeO₂/FCN composite was calculated by formula (1),

$$\text{Synergy factor}_{CeO_2/FCN-Photo-enzyme} = \frac{k_{CeO_2/FCN-Photo-enzyme}}{k_{CeO_2/FCN-Photo} + k_{CeO_2/FCN-Enzyme}} \quad (1)$$

and the calculated result was 1.33 (Table S3). If the synergy factor is greater than 1, it indicates that the combined system has a synergistic effect, which means that the performance of the combined system is
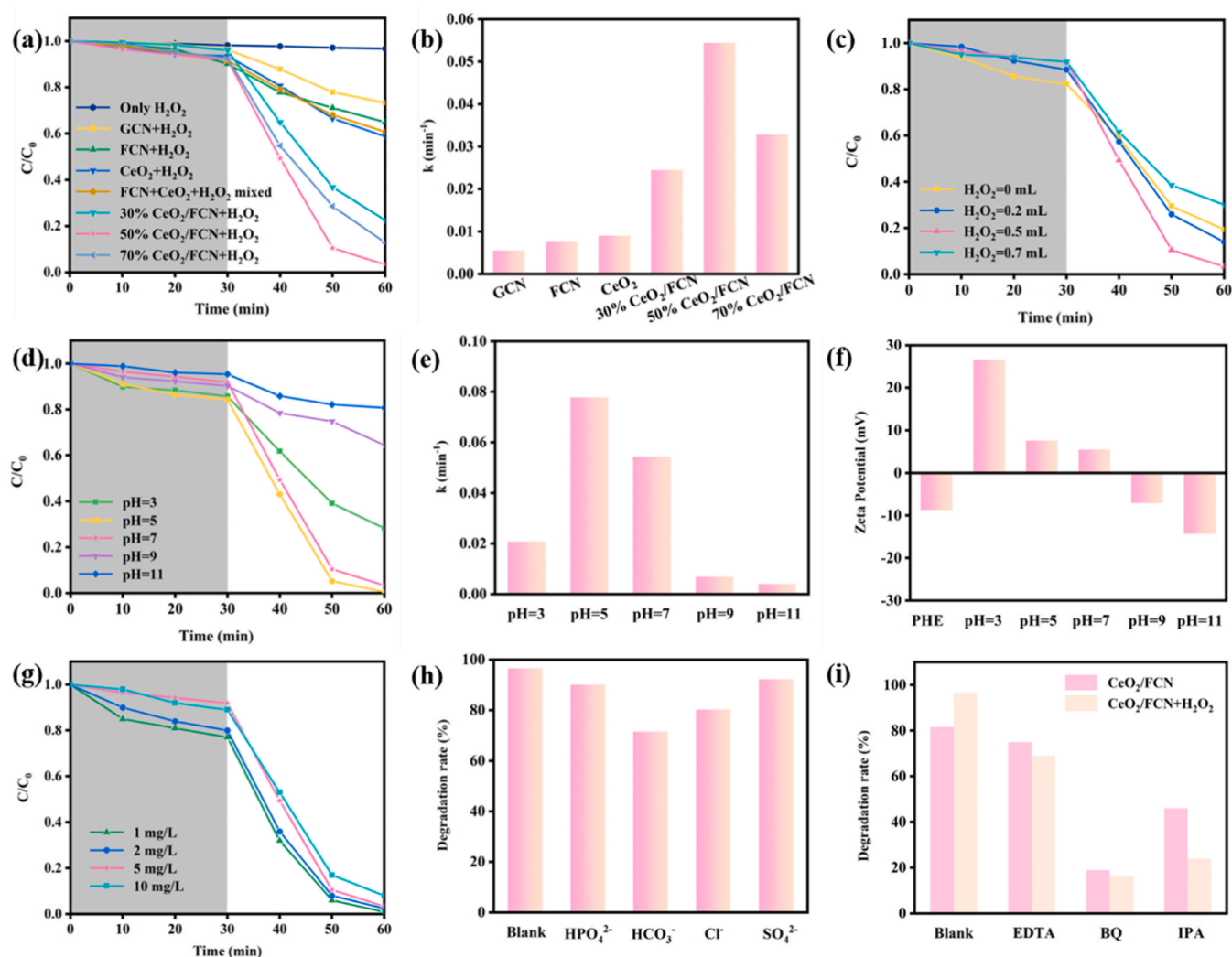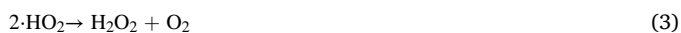
Fig. 5. (a) Performance and (b) standard rate constant of photo-enzyme synergistic catalytic degradation of PHE by different catalysts in the presence of H_2O_2; (c) photo-enzyme synergistic catalytic performance of CeO_2/FCN composite with different H_2O_2 addition; (d) Performance and (e) standard rate constant of photo-enzyme synergistic catalytic degradation under different pH conditions; (f) Zeta potential diagram of CeO_2/FCN composite at different pH values; (g) Effects of different PHE concentrations, (h) inorganic ions and (i) active species capture agents on degradation performance.

better than the sum of its individual components. Therefore, it is suggested that the photo-enzyme synergistic system is helpful to improve the catalytic degradation performance of CeO_2/FCN composite.

Fig. 5c shows the photo-enzyme synergistic catalytic activity of 50% CeO_2/FCN under different H_2O_2 supplemental levels. It can be found that the photocatalytic degradation efficiency of 50% CeO_2/FCN was about 80.6% when no H_2O_2 was added. With the addition of H_2O_2, the HRP activity of 50% CeO_2/FCN composite was stimulated, and the degradation efficiency of PHE was gradually improved through the synergistic effect of enzyme catalysis and photocatalysis. The degradation performance of 50% CeO_2/FCN composite reached the best when the addition amount of H_2O_2 was 0.5 mL. When excessive H_2O_2 is added, the degradation efficiency begins to decrease, possibly due to excess H_2O_2 becoming a scavenger of the active groups, thereby reducing catalytic activity. The specific reaction is shown in formula (2)-(4):

$$H_2O_2 + \cdot OH \rightarrow H_2O + \cdot HO_2 \tag{2}$$

$$2 \cdot HO_2 \rightarrow H_2O_2 + O_2 \tag{3}$$

$$\cdot HO_2 + \cdot OH \rightarrow H_2O + O_2 \tag{4}$$

Initial pH plays an important role in photo-enzyme synergistic catalysis. Fig. 5d shows the degradation effect of CeO_2/FCN composite on PHE under different pH conditions. In general, CeO_2/FCN composite can have higher photo-enzyme-catalyzed degradation effect under acidic conditions. It can be seen from Fig. 5e that the standard rate constant (k_{app}) of CeO_2/FCN composite is 0.05436 min^{-1} at pH= 7 and about 0.07781 min^{-1} at pH= 5. In addition, the degradation ability of CeO_2/FCN composite is poor under alkaline conditions, which may be related to electrostatic repulsion [36,37]. The Zeta potential test of CeO_2/FCN composite under different pH conditions (Fig. 5f) showed that it was mainly positively charged under acidic conditions but negatively charged under alkaline conditions. It is also worth noting that PHE itself is negatively charge. Therefore, under alkaline conditions, the CeO_2/FCN composite generates electrostatic repulsion with the PHE molecules, which prevents the interaction between the PHE and the CeO_2/FCN composite, thus reducing the degradation efficiency. At the same time, excessive OH^- will also inhibit·OH, resulting in reduced catalytic activity [38,39].

Subsequently, the effect of PHE solution at different concentrations on photo-enzyme synergistic catalysis was investigated. Fig. 5g shows that when the initial concentration is 1–5 mg/L, the photo-enzyme synergistic catalytic effect of CeO_2/FCN composite was more than

96% and it can be almost completely degraded. With the increase of concentration, the degradation effect decreased slightly, but it could still maintain above 90%. The decrease in degradation efficiency at higher concentrations of PHE solution may be due to two reasons. On the one hand, it may be because the number of active sites is insufficient under the same amount of catalyst to accommodate the increased concentrations of PHE. On the other hand, higher concentrations of PHE can lead to the production of more intermediates that compete with PHE for the active groups on the catalyst surface [40].

The influences of catalyst dosage on the PHE degradation efficiency were investigated and the results are presented in Fig. S2. It can be observed that the PHE degradation efficiency increases significantly from 51.1% to 96.6% within 60 min as the dosage of CeO$_2$/FCN composite is increased from 5 to 20 mg. This can be attributed to the production of a greater number of active species when the dosage of catalyst is increased [41]. However, the degradation efficiency was only slightly improved when the composite dosage was increased to 30 mg. Therefore, 20 mg of CeO$_2$/FCN composite was determined to be the optimal catalyst dosage for efficient PHE degradation.

In order to simulate the actual water environment, interference ions such as Cl$^-$, HCO$_3^-$, HPO$_4^{2-}$ and SO$_4^{2-}$ were added to PHE solution to explore their influence on the photo-enzyme synergistic catalytic degradation effect, and the results are shown in Fig. 5h. In general, CeO$_2$/FCN composites have good resistance to ion interference, and the photo-enzyme catalytic effect is almost unchanged. However, when HCO$_3^-$ and Cl$^-$ were added, the degradation effect decreased significantly. It is speculated that the addition of HCO$_3^-$ made the solution alkaline and formed electrostatic repulsion, which could interfere with the adsorption of PHE molecules on the catalyst surface [28,42]. Cl$^-$ can act as a scavenger for active species, inhibiting the active ingredient and reducing the catalytic activity [33,43].

In order to further study the main active groups of CeO$_2$/FCN composite, the active species capture experiments in the presence of H$_2$O$_2$ were respectively tested. It can be seen from Fig. 5i that the main active groups of CeO$_2$/FCN composite are·OH and·O$_2^-$. The subsequent comparison of the inhibition of the active groups in the presence of H$_2$O$_2$ showed that the inhibition rate of IPA on the photo-enzyme synergistic catalysis experiment was significantly increased, indicating that the addition of H$_2$O$_2$ was conducive to the generation of more·OH [6,44,45]. Therefore, it is considered that enzymatic reaction can significantly increase the catalytic degradation performance and form a photo-enzyme synergistic catalytic system.

3.4. Stability of CeO$_2$/FCN composite

The stability of the CeO$_2$/FCN composite is an important consideration. Firstly, the reusability of CeO$_2$/FCN composite was evaluated by a four-cycle photo-enzyme synergistic catalytic degradation of PHE. It can be seen from Fig. 6a that the catalytic effect of CeO$_2$/FCN composite remained almost unchanged after four cycles, indicating its good reusability. Subsequently, the cyclically degraded CeO$_2$/FCN composite was characterized by XRD, XPS, SEM and TEM (Fig. 6(b-e)). It was found that the chemical structure and microstructure of CeO$_2$/FCN composite did not change after degradation. In addition, the redox characteristics of CeO$_2$ allow for reversible transformation of its valence states during the catalytic cycle. After the catalytic cycle, the composite can be restored to its original state, ensuring its stability and reusability. This is an important feature that CeO$_2$/FCN composite can be used as a photo-enzyme synergistic catalytic material.

3.5. Possible degradation path of oxytetracycline and toxicity evaluation

In order to further study the intermediates that may be generated in the photo-enzyme synergistic catalytic degradation process, GC-MS was used for detection (Fig. S3, and possible intermediates are listed in Table S4. Fig. 7a describes the possible degradation paths in the photo-enzyme synergistic catalytic degradation of phenanthrene by CeO$_2$/FCN composite. Possible degradation paths for PHE under attack by·OH are described in Path I. Since the 9,10 double bond of PHE is the most electron-rich position, it is easy to attack to generate 9,10-phenanthrene
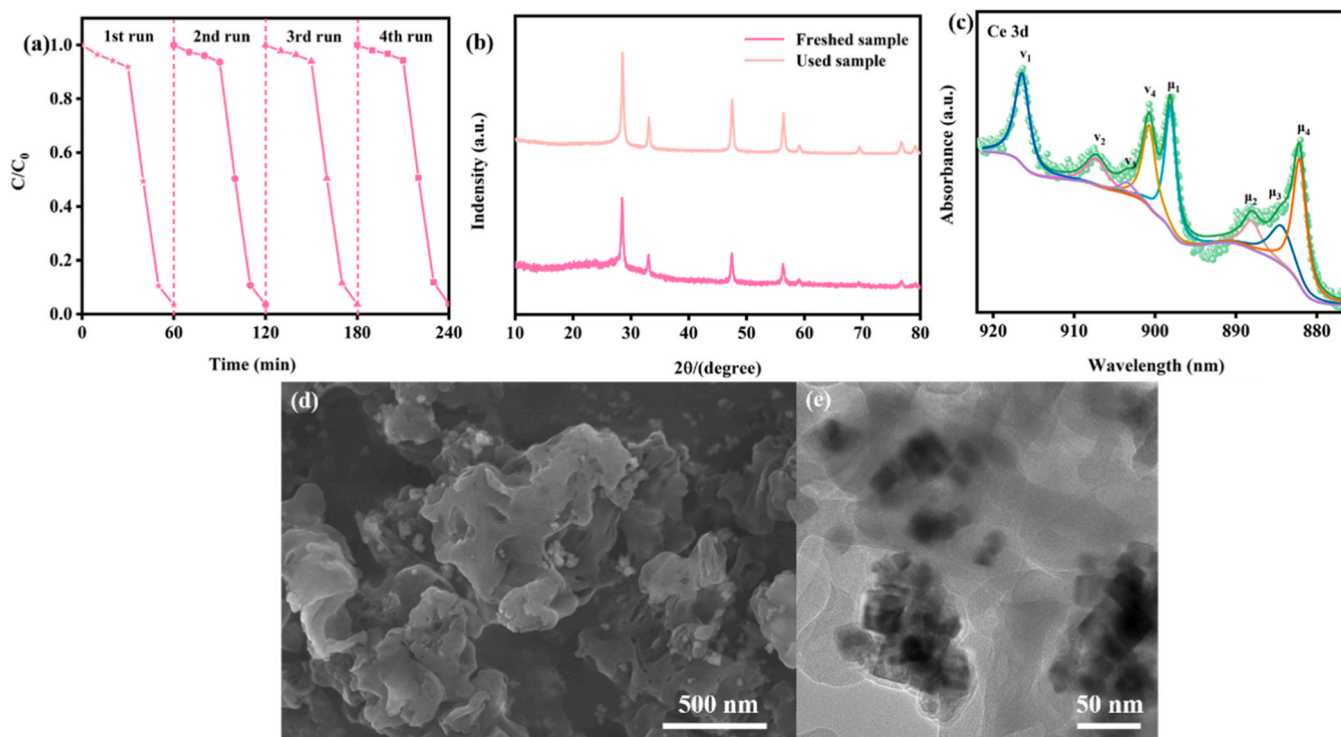
Fig. 6. (a) Experiments on photo-enzyme synergistic catalytic cycle of CeO$_2$/FCN composite; (b) XRD pattern of CeO$_2$/FCN composite before and after photocatalytic experiment; (c) XPS, (d) SEM and (e) TEM images of CeO$_2$/FCN composite after cyclic experiment.
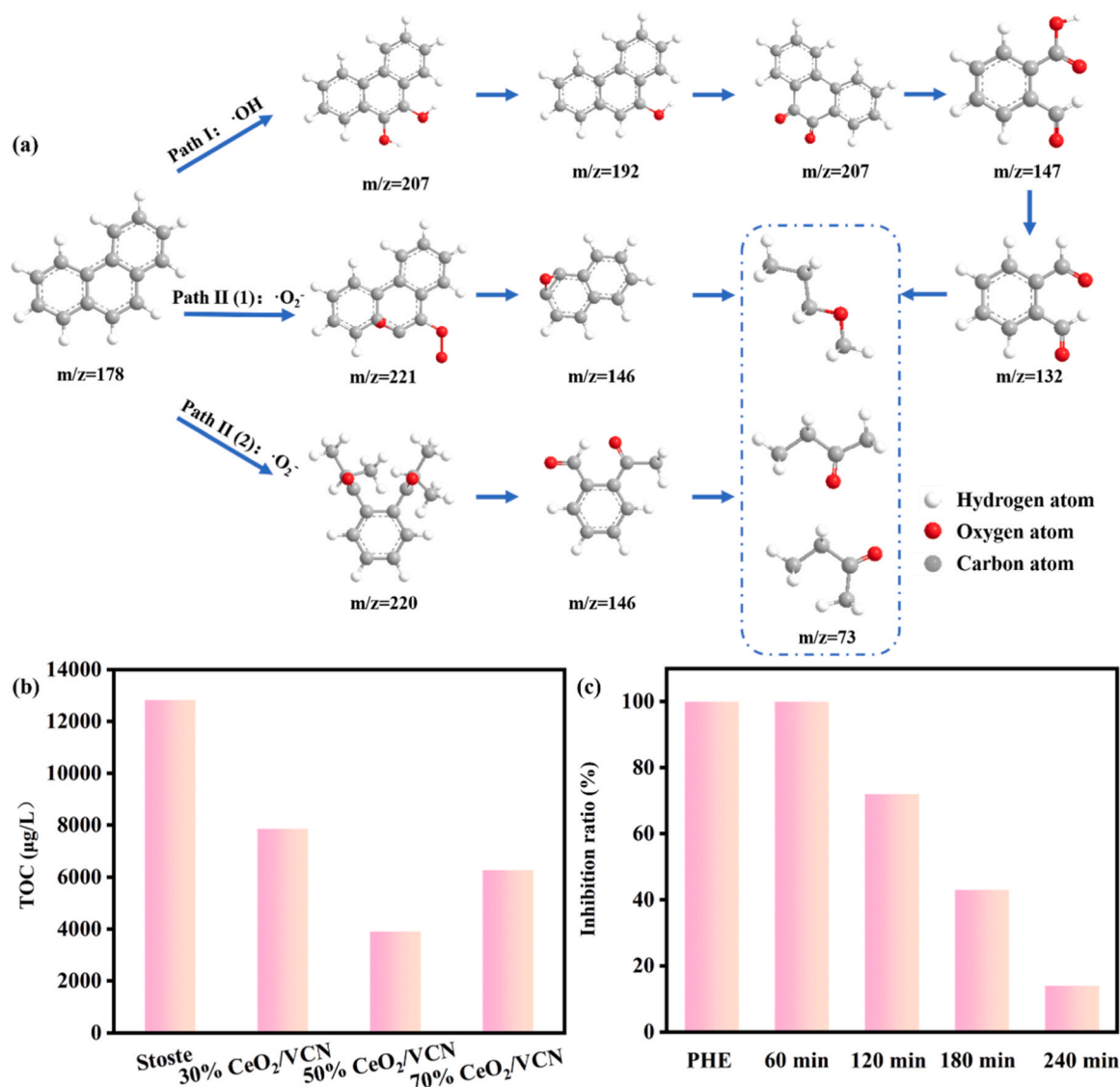
Fig. 7. (a) The proposed degradation pathway of PHE in CeO$_2$/FCN composite; (b) TOC concentration of different composites after degradation for 60 min and Toxicity test of CeO$_2$/FCN composite after degradation of different time.

glycol [2]; The second paths refer to that after the·O$_2^-$ attack, the double bond at position 10 of PHE is attacked to form intermediates, which dehydrate to form phenanthrene [9,10-b] oxime [3,5]. Over time, the concentration gradually decreases and new products are formed ($m/z = 146$ and 73). And the concentrations of these products ($m/z = 146$ and 73) rise with increasing reaction time. In these three paths, aromatic cyclic compounds such as phthalic acid, benzoic acid and bis (2-ethylbutyl) phthalate may be further obtained through peroxidation and ring-opening reaction, which are finally completely mineralized into small molecular compounds, H$_2$O and CO$_2$ with the progress of the reaction [1,28]. The TOC test showed that 50% CeO$_2$/FCN composite had the highest mineralization rate of about 70.1%, indicating its potential in mineralization ability (Fig. 7b). However, the toxicity assessment test (Fig. 7c) showed that the solution degraded by 50% CeO$_2$/FCN composite after 60 min still had a strong toxic effect on luminescent bacteria, possibly due to the rapid decomposition of aromatic cyclic compounds [3]. However, as the reaction progressed and these compounds were further mineralized into small organic acids, CO$_2$, and H$_2$O, the toxicity of the solution gradually decreased [40,46]. By the degradation time of 240 min, the toxicity of the solution was significantly reduced compared with that at 60 min,

indicating the potential of CeO$_2$/FCN composite in degrading toxic pollutants and promoting environmental remediation.

### 3.6. Optical and electrochemical characterization

The optical properties of GCN, FCN, CeO$_2$ and CeO$_2$/FCN composite were characterized by UV–visible diffuse reflection spectroscopy (DRS). As shown in Fig. 8a, the absorption edge of FCN is around 450 nm, and that of CeO$_2$ is about 420 nm. The prepared composite CeO$_2$/FCN has an absorption edge similar to that of FCN, and the absorption edge of CeO$_2$/FCN has an obvious redshift, which may be the result of the interaction between FCN and CeO$_2$. Then, the band gap of the prepared sample was calculated by formula (5) [47,48].

$$ahv = A\left(hv - E_g\right)^{n/2} \tag{5}$$

Among them, the band gap of FCN and CeO$_2$ is 2.86 eV and 2.95 eV, while the band gap of CeO$_2$/FCN is slightly smaller than that of FCN (2.84 eV), which is consistent with the trend of light absorption enhancement (Fig. 8b).

Generally speaking, the separation and transfer of photogenerated carrier will affect the photocatalytic performance [49,50]. Therefore,
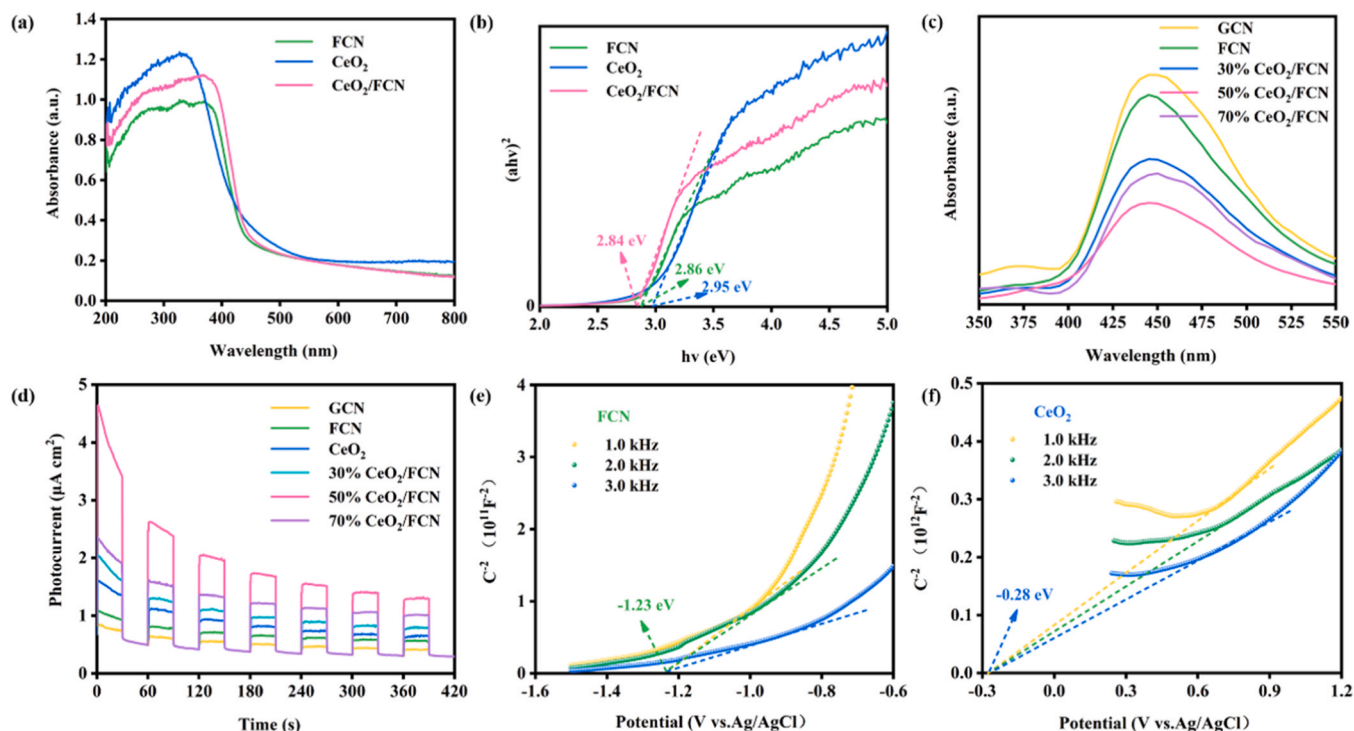
Fig. 8. (a) UV/vis absorption spectra, (b) Band-gap analysis diagram, (c) PL and (d) transient photocurrent response of the prepared catalysts and Mott−Schottky curves of (d)FCN and (f) CeO$_2$.

this study uses photoluminescence (PL) broad spectrum to study the process of semiconductor photoluminescence carrier separation and migration. Fig. 8c shows the luminescence spectra of GCN, FCN and a series of CeO$_2$/FCN composites at the excitation wavelength of 350 nm. Obviously, the photogenerated carrier recombination efficiency of CeO$_2$/FCN composite is significantly lower than that of pure sample. At the same time, 50% CeO$_2$/FCN composite has the lowest PL strength, which indicates that the introduction of CeO$_2$ can effectively reduce the photogenic electron hole pair recombination efficiency of FCN.

In addition, the separation and transfer behaviors of photogenerated electrons and holes in CeO$_2$/FCN composite were further characterized by transient photocurrent response experiments and electrochemical impedance experiments. It can be seen from Fig. 8d that compared with GCN, the recombination rate of photogenerated electrons and holes in FCN is reduced. Subsequently, among a series of CeO$_2$/FCN composites prepared after the introduction of CeO$_2$, 50% CeO$_2$/FCN composites have the lowest recombination rate of photogenerated electron hole pairs, which indicates that the separation and transfer of photogenerated electrons and holes in 50% CeO$_2$/FCN composite is faster and more efficient than that in pure samples [51,52]. Fig. S4 shows the electrochemical impedance diagram of the prepared sample. Obviously, the semicircle diameter of 50% CeO$_2$/FCN is smaller than that of FCN and CeO$_2$, which means that the charge transfer resistance of CeO$_2$/FCN is smaller and the charge transfer rate is faster [50]. Based on the comparison of these photochemical properties, it was determined that the 50% CeO$_2$/FCN composite has high photogenic electron separation efficiency, which is considered to be the reason for its highest photo-enzyme synergistic catalytic activity.

3.7. Mechanism of the photo-enzyme synergistic catalytic activities for CeO$_2$/FCN heterojunction

In order to further understand the band structure of the semiconductor, Mott-Schottky tests were performed on FCN and CeO$_2$ to determine the conduction band location, and the valence band location was determined by formula (6) [53,54].

$$E_{VB} = E_g + E_{CB} \tag{6}$$

It can be seen from Fig. 8(e, f) that the M-S curves of FCN and CeO$_2$ show a positive slope, which indicates that both FCN and CeO$_2$ are n-type semiconductor materials. The flat band potential (E$_{fb}$) of FCN and CeO$_2$ were determined to be − 1.23 eV and − 0.28 eV, respectively. In n-type semiconductor materials, the conduction band edge (E$_{CB}$) is associated with the Ag/AgCl electrode and its potential is typically more negative than that of the hydrogen electrode by about 0.2 eV. Therefore, according to formula (7),

$$E_{NHE} = E_{Ag/AgCl} + 0.197 eV \tag{7}$$

the E$_{CB}$ positions of FCN and CeO$_2$ are calculated as − 1.03 eV and − 0.08 eV, respectively. Then, the E$_{VB}$ positions were determined by formula (2), corresponding to 1.83 eV and 2.87 eV, respectively [55–57].

In addition, in order to further confirm the main active groups in CeO$_2$/FCN composite, low-temperature spin resonator (ESR) was used for testing. In Fig. 9a, it can be found that there are six obvious typical signal peaks in ESR spectrum under illumination conditions, which can be attributed to·O$_2^-$ [23]. Meanwhile, the peak intensity of·O$_2^-$ increases gradually with the increase of illumination time. The presence or absence of H$_2$O$_2$ in the test conditions also affected the ESR spectrum (Fig. 9b). Without H$_2$O$_2$, there was no·OH signal peak in the CeO$_2$/FCN composite under dark conditions. However, after the introduction of xenon lamp, four typical peaks gradually appeared and peak intensity accumulated with the increase of illumination time [7]. By comparing the peak intensity after adding H$_2$O$_2$, it was found that the intensity of the four typical peaks of·OH was significantly higher than that without H$_2$O$_2$. Therefore, it was concluded that the introduction of H$_2$O$_2$ can generate more·OH, effectively forming a photo-enzyme synergistic catalytic system, and improving the degradation effect of PHE.

The work function of FCN and CeO$_2$ was calculated by ultraviolet photoelectron spectroscopy (UPS), which can gain insights into the electron transfer pathways at the heterojunction interface. As shown in
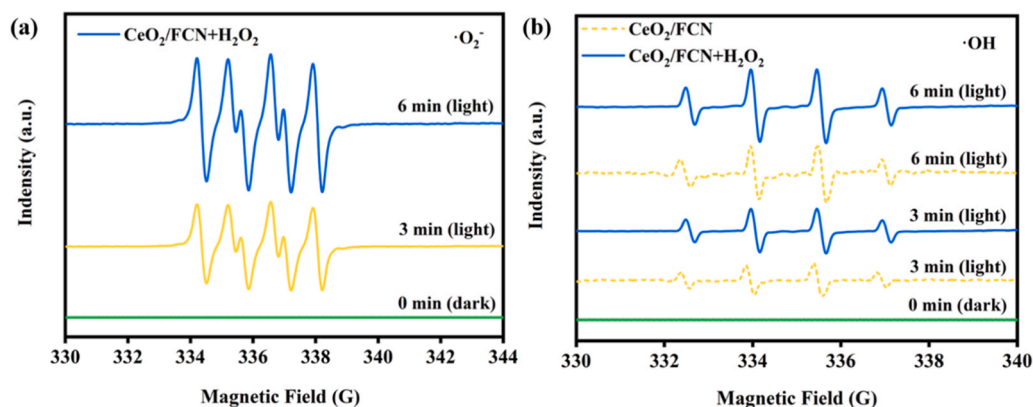
Fig. 9. (a) ESR spectra of CeO$_2$/FCN composite for·O$_2^-$ and·OH under different conditions.
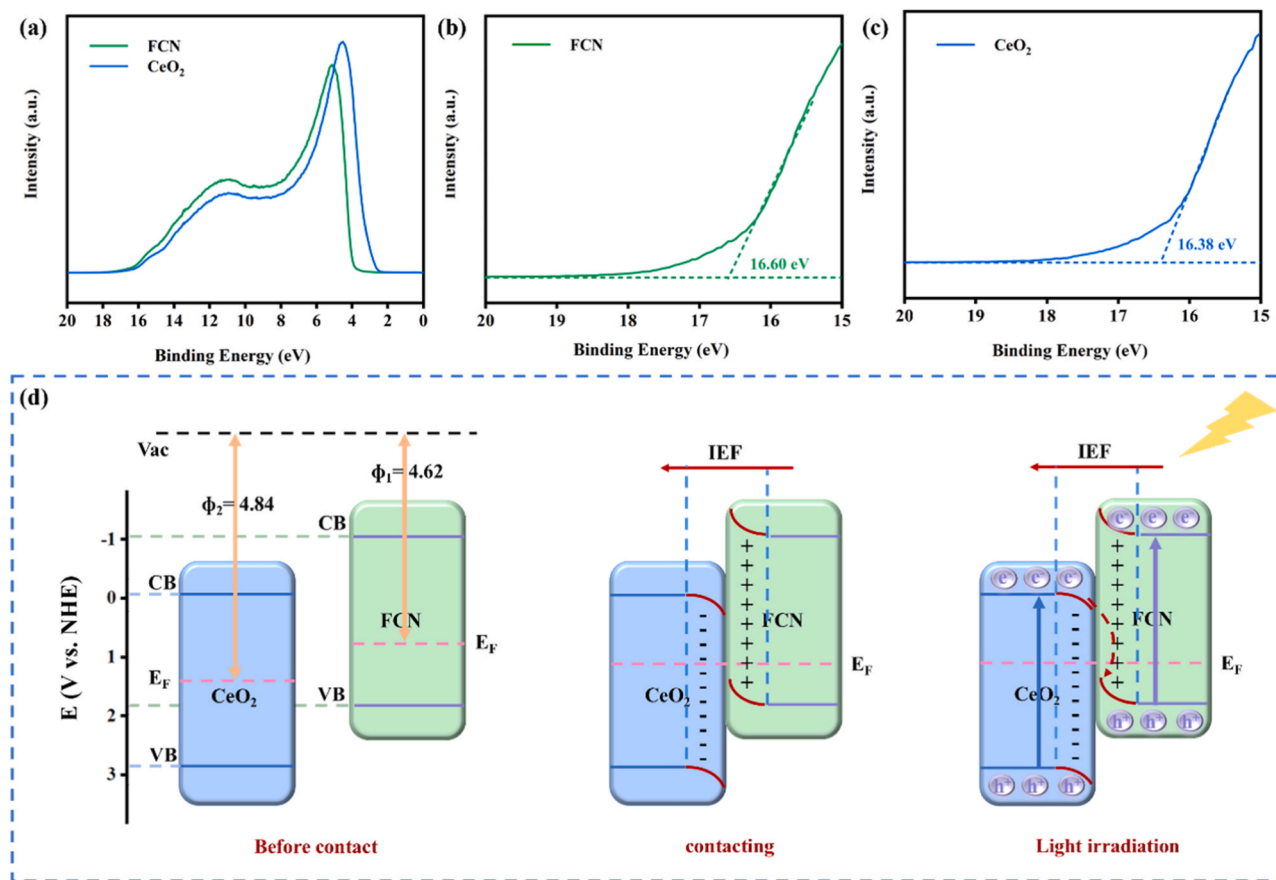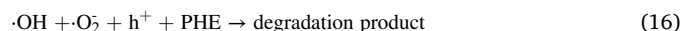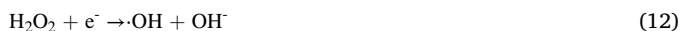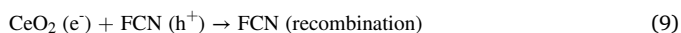

Fig. 10. (a-c) UPS spectra of the pristine FCN and CeO$_2$; (d) Relative energy band positions and S-scheme charge transfer mechanism between pristine the pristine FCN and CeO$_2$.

Fig. 10(a-c), the cut-off energy values (E$_c$) of FCN and CeO$_2$ are 16.60 eV and 16.38 eV, respectively. The work function values of FCN and CeO$_2$ were obtained by subtracting the excitation energy of He I excitation energy (21.22 eV), which were 4.62 eV and 4.84 eV. According to Fig. 10d, there is a staggered band relationship between FCN and CeO$_2$, and FCN has a higher Fermi energy level. As a result, when FCN and CeO$_2$ come into contact, electrons in FCN will tend to move spontaneously towards CeO$_2$ until the Fermi level between them is balanced, generating an internal electric field (IEF) at the interface [29,58]. At the same time, the interfacial band of FCN is bent upward due to the loss of electrons, while the interfacial band of CeO$_2$ is bent downward due to the accumulation of electrons. This interfacial band bending at the heterojunction interface can effectively control the one-way flow of photogenerated electrons and hole [29,41]. This action can promote the transfer of electrons from CeO$_2$ to FCN, while hindering the transfer of holes from FCN to CeO$_2$, which can preserve the electrons in the conduction band of FCN and the holes in the valence band of CeO$_2$. Under light conditions, the electrons in the conduction band of CeO$_2$ are rapidly transferred to the valence band of FCN, where they can recombine with the holes under the combined action of the IEF and interfacial band bending. This promotes the separation and migration of photogenerated charge carriers, enhancing the photocatalytic activity of the heterojunction. Furthermore, the photogenerated electron-hole pair separation efficiency and redox capacity of the S-type heterojunction are

higher than those of the traditional type II heterojunction.

Combined with all experimental results, a possible mechanism for photo-enzyme synergistic catalytic degradation of PHE by CeO$_2$/FCN composite was proposed, as shown in Scheme 2. Under the illumination of ultraviolet light, the IEF of S-scheme causes the photogenerated electron hole pairs to be continuously separated. After being separated by the IEF, the e$^-$ on the CB of CeO$_2$ is transferred to the VB of the FCN and recombined with the h$^+$ on the VB, while the h$^+$ in the VB of CeO$_2$ is retained, which can oxidize OH$^-$ or H$_2$O to·OH (OH$^-$/·OH 1.99 eV, H$_2$O/ ·OH 2.68 eV) [24,28]. At the same time, the CB potential energy of FCN (−1.03 eV) is much lower than that of O$_2$/·O$_2^-$ (−0.33 eV), so e$^-$ in FCN can restore O$_2$ generation·O$_2^-$ [33]. In addition, CeO$_2$/FCN composite has the HRP activity. After adding H$_2$O$_2$ into the solution, Ce will undergo redox cycle reaction, which means that more·OH can be generated by changing the electronic structure and oxidation state of Ce^{4+}/Ce^{3+}. This is similar to the Fenton-like reaction of Fe. Ce^{4+} can not only capture e$^-$ and reduce to Ce^{3+} (Ce^{3+}/Ce^{4+}=1.44 eV), but also reduce to Ce^{3+} via H$_2$O$_2$ [59]. The reduced Ce^{3+} can directly decompose H$_2$O$_2$ to produce·OH and generate Ce^{4+}, which restores the activated enzyme to its initial state and completes a catalytic cycle. During the cycle, part of the e$^-$ can break down the H$_2$O$_2$ into·OH [26,60]. Finally,·OH,·O$_2^-$ and h$^+$ will participate in the catalytic degradation of PHE. Based on the above discussion, it can be found that combining CeO$_2$ and FCN to construct S-scheme heterojunction can effectively inhibit the recombination rate of photogenerated electron hole pairs and improve the photocatalytic efficiency. At the same time, due to the properties of CeO$_2$ to activate hydroxides, CeO$_2$/FCN composite can effectively activate H$_2$O$_2$ to generate more·OH, which will contribute to the photo-enzyme synergistic catalytic degradation of PHE. The specific reaction can be illustrated by the Eqs. (8)-(16):

$$CeO_2/FCN + hv \rightarrow CeO_2\ (e^-+h^+)/FCN\ (e^-+h^+) \tag{8}$$

$$CeO_2\ (e^-) + FCN\ (h^+) \rightarrow FCN\ (recombination) \tag{9}$$

$$FCN\ (e^-) + O_2 \rightarrow ·O_2^- \tag{10}$$

$$CeO_2\ (h^+) + OH^-/H_2O \rightarrow ·OH \tag{11}$$

$$H_2O_2 + e^- \rightarrow ·OH + OH^- \tag{12}$$

$$Ce^{4+} + e^- \rightarrow Ce^{3+} \tag{13}$$

$$Ce^{4+} + H_2O_2 \rightarrow Ce^{3+} + HO_2^. + H^+ \tag{14}$$

$$Ce^{3+} + H_2O_2 \rightarrow Ce^{4+} + ·OH + HO^- \tag{15}$$

$$·OH + ·O_2^- + h^+ + PHE \rightarrow degradation\ product \tag{16}$$

4. Conclusions

In this study, the porous foveolate g-C$_3$N$_4$ were combined with CeO$_2$ with horseradish peroxidase activity by ultrasonic impregnation method to prepare S-scheme CeO$_2$/FCN heterojunction, which could realize the photo-enzyme synergistic catalytic reaction. Firstly, the strong redox capacity of the CeO$_2$/FCN composite was retained through S-scheme heterojunction, and then the redox electron transfer between Ce^{4+}/Ce^{3+} was achieved through the HRP activity to generate more·OH, which effectively improved the catalytic capacity of the composite. In addition, ESR experiments confirmed that·OH is not only derived from H$_2$O$_2$, but also effectively generated in the photocatalytic reaction system. Therefore, it is considered that the CeO$_2$/FCN composite has realized the photo-enzyme synergistic catalytic performance, which will provide important technology and basic knowledge for the future PAHs wastewater purification methods.

CRediT authorship contribution statement

Chujun Feng: Data curation, Formal analysis, Writing – review & editing. **Jian Rong**: Data curation, Formal analysis. **Yuzhe Zhang**: Methodology, Writing – original draft. **Xudong Zheng**: Writing – review & editing, Supervision. **Xiazhang Li**: Writing – original draft. **Song Xu**: Formal analysis, Writing – review & editing, Supervision. **Zhongyu Li**: Project administration, Supervision, Funding acquisition.

Declaration of Competing Interest
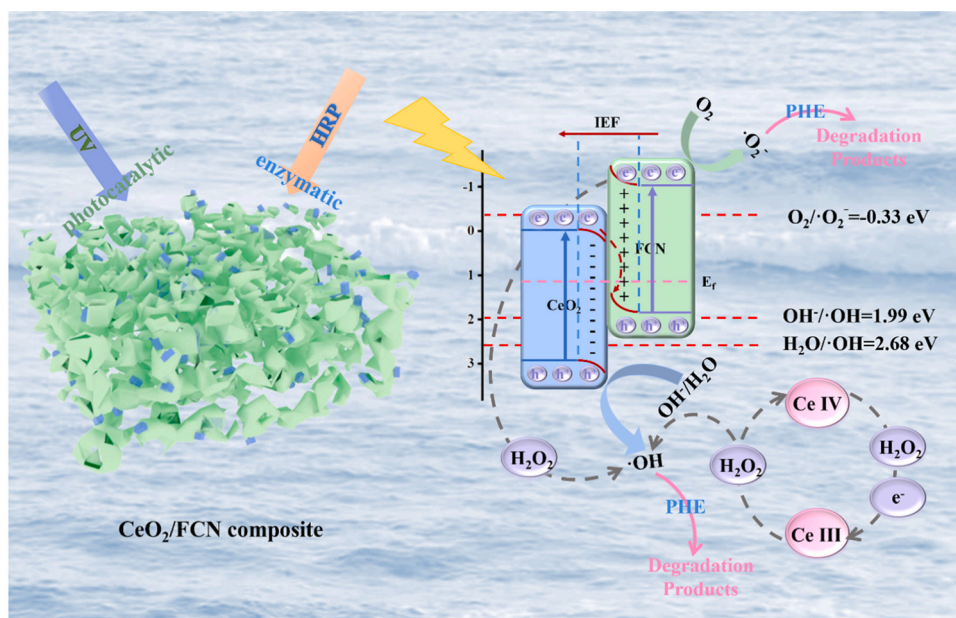
Scheme 2. Mechanism diagram of photo-enzyme synergistic catalytic over CeO$_2$/FCN S-scheme heterojunction.

Data Availability

Data will be made available on request.

Appendix A. Supporting information

Supplementary data associated with this article can be found in the online version at doi:10.1016/j.apcatb.2023.123005.

References

[1] Q. Shang, M. Tan, J. Chi, Effects of biodegradable and non-degradable microplastics on microbial availability and degradation of phenanthrene in soil, J. Environ. Chem. Eng. 10 (2022), 108832.

[2] H. Ji, W. Liu, F. Sun, T. Huang, L. Chen, Y. Liu, J. Qi, C. Xie, D. Zhao, Experimental evidences and theoretical calculations on phenanthrene degradation in a solar-light-driven photocatalysis system using silica aerogel supported TiO_2 nanoparticles: insights into reactive sites and energy evolution, Chem. Eng. J. 419 (2021), 129605.

[3] H. Lee, H. Anwer, J.W. Park, Graphene quantum dots on stainless-steel nanotubes for enhanced photocatalytic degradation of phenanthrene under visible light, Chemosphere 246 (2020), 125761.

[4] Z. Cai, X. Hao, X. Sun, P. Du, W. Liu, J. Fu, Highly active $WO_3@anatase-SiO_2$ aerogel for solar-light-driven phenanthrene degradation: mechanism insight and toxicity assessment, Water Res. 162 (2019) 369–382.

[5] K. Cheng, Z. Cai, J. Fu, X. Sun, W. Sun, L. Chen, D. Zhang, W. Liu, Synergistic adsorption of Cu(II) and photocatalytic degradation of phenanthrene by a jaboticaba-like TiO_2/titanate nanotube composite: an experimental and theoretical study, Chem. Eng. J. 358 (2019) 1155–1165.

[6] J. Bian, X. An, W. Jiang, R. Liu, C. Hu, H. Liu, Defect-enhanced activation of carbon nitride/horseradish peroxidase nanohybrids for visible-light-driven photobiocatalytic water purification, Chem. Eng. J. 408 (2021), 127231.

[7] L. Wang, Z. Yang, G. Song, Z. You, X. Zhang, L. Liu, J. Zhang, L. Ding, N. Ren, A. Wang, J. Liu, H. Liu, X. Yu, Construction of S-N-C bond for boosting bacteria-killing by synergistic effect of photocatalysis and nanozyme, Appl. Catal. B: Environ. 325 (2023), 122345.

[8] M. Guo, F. Gu, L. Meng, Q. Liao, Z. Meng, W. Liu, Synthesis of formaldehyde from CO_2 catalyzed by the coupled photo-enzyme system, Sep. Purif. Technol. 286 (2022), 120480.

[9] Y. Zhang, X. Cao, Y. Yang, S. Guan, X. Wang, H. Li, X. Zheng, L. Zhou, Y. Jiang, J. Gao, Visible light assisted enzyme-photocatalytic cascade degradation of organophosphorus pesticides, Green. Chem. 4 (2023) 30–38.

[10] F.K. de Oliveira, L.O. Santos, J.G. Buffon, Mechanism of action, sources, and application of peroxidases, Food Res. Int. 143 (2021), 110266.

[11] W. Jiang, J. Yang, X. Wang, H. Han, Y. Yang, J. Tang, Q. Li, Phenol degradation catalyzed by a peroxidase mimic constructed through the grafting of heme onto metal-organic frameworks, Bioresour. Technol. 247 (2018) 1246–1248.

[12] W. Cai, F. Chen, X. Shen, L. Chen, J. Zhang, Enhanced catalytic degradation of AO7 in the CeO_2–H_2O_2 system with Fe^{3+} doping, Appl. Catal. B Environ. 101 (2010) 160–168.

[13] F. Chen, X. Shen, Y. Wang, J. Zhang, CeO_2/H_2O_2 system catalytic oxidation mechanism study via a kinetics investigation to the degradation of acid orange 7, Appl. Catal. B: Environ. 121–122 (2012) 223–229.

[14] F.-X. Wang, C.-C. Wang, X. Du, Y. Li, F. Wang, P. Wang, Efficient removal of emerging organic contaminants via photo-Fenton process over micron-sized Fe-MOF sheet, Chem. Eng. J. 429 (2022), 132495.

[15] D. Wang, C. Gong, H. Zhao, Au NPs@NC@MnO_2 with exceptional nano-enzyme activity for sensitive colorimetric detection of Cr (VI), Microchem. J. 181 (2022), 107706.

[16] W. Yang, C. Weng, X. Li, H. He, J. Fei, W. Xu, X. Yan, W. Zhu, H. Zhang, X. Zhou, A sensitive colorimetric sensor based on one-pot preparation of h-Fe_3O_4@ppy with high peroxidase-like activity for determination of glutathione and H_2O_2, Sens. Actuators B: Chem. 338 (2021), 129844.

[17] S. Di, J. Wang, Y. Zhai, P. Chen, T. Ning, C. Shi, H. Yang, Y. Bao, Q. Gao, S. Zhu, Efficient activation of peroxymonosulfate mediated by Co(II)-CeO_2 as a novel heterogeneous catalyst for the degradation of refractory organic contaminants: degradation pathway, mechanism and toxicity assessment, J. Hazard. Mater. 435 (2022), 129013.

[18] F. Chen, Q. Yang, Y. Wang, J. Zhao, D. Wang, X. Li, Z. Guo, H. Wang, Y. Deng, C. Niu, G. Zeng, Novel ternary heterojunction photococatalyst of Ag nanoparticles and g-C_3N_4 nanosheets co-modified $BiVO_4$ for wider spectrum visible-light photocatalytic degradation of refractory pollutant, Appl. Catal. B: Environ. 205 (2017) 133–147.

[19] C.X. Zhao, Y.Z. Zhang, H.L. Jiang, J. Chen, Y. Liu, Q. Liang, M. Zhou, Z.Y. Li, Y. T. Zhou, Combined effects of octahedron NH_2-UiO-66 and flowerlike $ZnIn_2S_4$

[20] microspheres for photocatalytic dye degradation and hydrogen evolution under visible light, J. Phys. Chem. C. 123 (2019) 18037–18049.

[20] S. Fang, Y. Zhou, M. Zhou, Z. Li, S. Xu, C. Yao, Facile synthesis of novel $ZnFe_2O_4$/CdS nanorods composites and its efficient photocatalytic reduction of Cr(VI) under visible-light irradiation, J. Ind. Eng. Chem. 58 (2018) 64–73.

[21] H. Li, X. Li, J. Zhou, W. Sheng, X. Lang, Extending aromatic acids on TiO_2 for cooperative photocatalysis with triethylamine: violet light-induced selective aerobic oxidation of sulfides, Chin. Chem. Lett. 33 (2022) 3733–3738.

[22] M. Xin, Fulin Zhang, Yuexin Wang, Xiaoyun Dong, Xianjun Lang, 2D β-ketoenamine-linked triazine covalent organic framework photocatalysis for selective oxidation of sulfides, Sustain. Energy Fuels 7 (2023) 1963–1973.

[23] K. Wang, Z. Xing, D. Meng, S. Zhang, Z. Li, K. Pan, W. Zhou, Hollow $MoSe_2$@Bi_2S_3/CdS core-shell nanostructure as dual z-scheme heterojunctions with enhanced full spectrum photocatalytic-photothermal performance, Appl. Catal. B: Environ. 281 (2021), 119482.

[24] Y. Guo, Y. Ao, P. Wang, C. Wang, Mediator-free direct dual-Z-scheme $Bi_2S_3/BiVO_4$/$MgIn_2S_4$ composite photocatalysts with enhanced visible-light-driven performance towards carbamazepine degradation, Appl. Catal. B: Environ. 254 (2019) 479–490.

[25] L. Jiang, X. Yuan, G. Zeng, J. Liang, X. Chen, H. Yu, H. Wang, Z. Wu, J. Zhang, T. Xiong, In-situ synthesis of direct solid-state dual Z-scheme WO_3/g-C_3N_4/Bi_2O_3 photocatalyst for the degradation of refractory pollutant, Appl. Catal. B: Environ. 227 (2018) 376–385.

[26] W. Zhao, Z. Wei, X. Zhang, M. Ding, S. Huang, S. Yang, Magnetic recyclable $MnFe_2O_4$/CeO_2/SnS_2 ternary nano-photocatalyst for photo-Fenton degradation, Appl. Catal. A: Gen. 593 (2020), 117443.

[27] Y. Wang, W. Yang, X. Chen, J. Wang, Y. Zhu, Photocatalytic activity enhancement of core-shell structure g-C_3N_4@TiO_2 via controlled ultrathin g-C_3N_4 layer, Appl. Catal. B: Environ. 220 (2018) 337–347.

[28] C. Feng, Q. Gu, J. Rong, Q. Liang, M. Zhou, X. Li, S. Xu, Z. Li, Porous dual Z-scheme InOOH/RCN/CoWO$_4$ heterojunction with enhanced photothermal-photocatalytic properties towards norfloxacin degradation, Sep. Purif. Technol. 308 (2023), 122890.

[29] Y. Shi, L. Li, Z. Xu, F. Guo, W. Shi, Construction of full solar-spectrum available S-scheme heterojunction for boosted photothermal-assisted photocatalytic H_2 production, Chem. Eng. J. 459 (2023), 141549.

[30] X. Sun, Y. Shi, J. Lu, W. Shi, F. Guo, Template-free self-assembly of three-dimensional porous graphitic carbon nitride nanovesicles with size-dependent photocatalytic activity for hydrogen evolution, Appl. Surf. Sci. 606 (2022), 154841.

[31] Z. Tan, G. Li, H.-L. Chou, Y. Li, X. Yi, A.H. Mahadi, A. Zheng, S.C. Edman Tsang, Y.-K. Peng, Differentiating Surface Ce Species among CeO_2 Facets by Solid-State NMR for Catalytic Correlation, ACS Catal. 10 (2020) 4003–4011.

[32] Y. Jiao, Q. Huang, J. Wang, Z. He, Z. Li, A novel MoS_2 quantum dots (QDs) decorated Z-scheme g-C_3N_4 nanosheet/N-doped carbon dots heterostructure photocatalyst for photocatalytic hydrogen evolution, Appl. Catal. B: Environ. 247 (2019) 124–132.

[33] C.J. Feng, Y.N. Wang, Z.W. Lu, Q. Liang, Y.Z. Zhang, Z.Y. Li, S. Xu, Nanoflower Ni_5P_4 coupled with GCNQDs as Schottky junction photocatalyst for the efficient degradation of norfloxacin, Sep. Purif. Technol. 282 (2022), 120107.

[34] R. Zhou, R. Zhou, D. Alam, T. Zhang, W. Li, Y. Xia, A. Mai-Prochnow, H. An, E. C. Lovell, H. Masood, R. Amal, K. Ostrikov, P.J. Cullen, Plasmacatalytic bubbles using CeO_2 for organic pollutant degradation, Chem. Eng. J. 403 (2021), 126413.

[35] S. Cai, J. Liu, J. Ding, Z. Fu, H. Li, Y. Xiong, Z. Lian, R. Yang, C. Chen, Tumor-microenvironment-responsive cascade reactions by a cobalt-single-atom nanozyme for synergistic nanocatalytic chemotherapy, Angew. Chem. Int. Ed. Engl. 61 (2022) e202204502.

[36] N. Yin, H. Chen, X. Yuan, Y. Zhang, M. Zhang, J. Guo, Y. Zhang, L. Qiao, M. Liu, K. Song, Highly efficient photocatalytic degradation of norfloxacin via $Bi_2Sn_2O_7$/PDIH Z-scheme heterojunction: influence and mechanism, J. Hazard. Mater. 436 (2022), 129317.

[37] Z. Yang, Y. Li, X. Zhang, X. Cui, S. He, H. Liang, A. Ding, Sludge activated carbon-based $CoFe_2O_4$-SAC nanocomposites used as heterogeneous catalysts for degrading antibiotic norfloxacin through activating peroxymonosulfate, Chem. Eng. J. 384 (2020), 123319.

[38] W. Liu, J. Zhou, Z. Hu, Nano-sized g-C_3N_4 thin layer @ CeO_2 sphere core-shell photocatalyst combined with H_2O_2 to degrade doxycycline in water under visible light irradiation, Sep. Purif. Technol. 227 (2019), 115665.

[39] W. Zhang, Z. Bian, X. Xin, L. Wang, X. Geng, H. Wang, Comparison of visible light driven H_2O_2 and peroxymonosulfate degradation of norfloxacin using Co/g-C_3N_4, Chemosphere 262 (2021), 127955.

[40] C.J. Feng, Z.W. Lu, Y.Z. Zhang, Q. Liang, M. Zhou, X.Z. Li, C. Yao, Z.Y. Li, S. Xu, A magnetically recyclable dual Z-scheme GCNQDs-$CoTiO_3$/$CoFe_2O_4$ composite photocatalyst for efficient photocatalytic degradation of oxytetracycline, Chem. Eng. J. 435 (2022), 134833.

[41] S. Li, C. Wang, M. Cai, F. Yang, Y. Liu, J. Chen, P. Zhang, X. Li, X. Chen, Facile fabrication of TaON/Bi_2MoO_6 core–shell S-scheme heterojunction nanofibers for boosting visible-light catalytic levofloxacin degradation and Cr(VI) reduction, Chem. Eng. J. 428 (2022), 131158.

[42] J.S. Liu, C.J. Feng, Y. Li, Y.Z. Zhang, Q. Liang, S. Xu, Z.Y. Li, S.M. Wang, Photocatalytic detoxification of hazardous pymetrozine pesticide over two-dimensional covalent-organic frameworks coupling with Ag_3PO_4 nanospheres, Sep. Purif. Technol. 288 (2022), 120644.

[43] J. Li, Z. Xia, D. Ma, G. Liu, N. Song, D. Xiang, Y. Xin, G. Zhang, Q. Chen, Improving photocatalytic activity by construction of immobilized Z-scheme CdS/Au/TiO_2 nanobelt photocatalyst for eliminating norfloxacin from water, J. Colloid Interface Sci. 586 (2021) 243–256.

[44] W. Lu, Y. Guo, J. Zhang, Y. Yue, L. Fan, F. Li, C. Dong, S. Shuang, A. High, Catalytic activity nanozyme based on cobalt-doped carbon dots for biosensor and anticancer cell effect, ACS Appl. Mater. Interfaces 14 (2022) 57206–57214.

[45] P.K. Boruah, G. Darabdhara, M.R. Das, Polydopamine functionalized graphene sheets decorated with magnetic metal oxide nanoparticles as efficient nanozyme for the detection and degradation of harmful triazine pesticides, Chemosphere 268 (2021), 129328.

[46] J. Ji, X. Sun, W. He, Y. Liu, J. Duan, W. Liu, L.D. Nghiem, Q. Wang, Z. Cai, Built-in electric field enabled in carbon-doped Bi_3O_4Br nanocrystals for excellent photodegradation of PAHs, Sep. Purif. Technol. 302 (2022), 122066.

[47] F. Guo, J. Chen, J. Zhao, Z. Chen, D. Xia, Z. Zhan, Q. Wang, Z-scheme heterojunction g-C_3N_4@PDA/BiOBr with biomimetic polydopamine as electron transfer mediators for enhanced visible-light driven degradation of sulfamethoxazole, Chem. Eng. J. 386 (2020), 124014.

[48] H. Guo, C.-G. Niu, L. Zhang, X.-J. Wen, C. Liang, X.-G. Zhang, D.-L. Guan, N. Tang, G.-M. Zeng, Construction of direct Z-scheme AgI/$Bi_2Sn_2O_7$ nanojunction system with enhanced photocatalytic activity: accelerated interfacial charge transfer induced efficient Cr(VI) reduction, tetracycline degradation and escherichia coli inactivation, ACS Sustain. Chem. Eng. 6 (2018) 8003–8018.

[49] C. Jiang, H. Wang, Y. Wang, H. Ji, All solid-state Z-scheme CeO_2/$ZnIn_2S_4$ hybrid for the photocatalytic selective oxidation of aromatic alcohols coupled with hydrogen evolution, Appl. Catal. B: Environ. 277 (2020), 119235.

[50] Y. Li, K. Lv, W. Ho, F. Dong, X. Wu, Y. Xia, Hybridization of rutile TiO2 (rTiO2) with g-C3N4 quantum dots (CN QDs): an efficient visible-light-driven Z-scheme hybridized photocatalyst, Appl. Catal. B: Environ. 202 (2017) 611–619.

[51] Q. Liang, W. Gao, C. Liu, S. Xu, Z.Y. Li, A novel 2D/1D core-shell heterostructures coupling MOF-derived iron oxides with $ZnIn_2S_4$ for enhanced photocatalytic activity, J. Hazard. Mater. 392 (2020), 122500.

[52] D. Liu, D. Chen, N. Li, Q. Xu, H. Li, J. He, J. Lu, Integration of 3D macroscopic graphene aerogel with 0D–2D AgVO3-g-C3N4 heterojunction for highly efficient photocatalytic oxidation of nitric oxide, Appl. Catal. B: Environ. 243 (2019) 576–584.

[53] Q. Liang, C. Zhang, S. Xu, M. Zhou, Z. Li, Nanocomposites based on 3D honeycomb-like carbon nitride with $Cd_{0.5}Zn_{0.5}S$ quantum dots for efficient photocatalytic hydrogen evolution, Int. J. Hydrog. Energy 44 (2019) 29964–29974.

[54] X.H. Zhao, Y.T. Zhou, Q. Liang, M. Zhou, Z.Y. Li, S. Xu, Coupling MOF-derived titanium oxide with $CdIn_2S_4$ formed 2D/3D core–shell heterojunctions with enhanced photocatalytic performance, Sep. Purif. Technol. 279 (2021), 119765.

[55] X.H. Zhao, Y. Xu, X.H. Wang, Q. Liang, M. Zhou, S. Xu, Z.Y. Li, Construction and enhanced efficiency of Z-scheme-based ZnCdS/Bi_2WO_6 composites for visible-light-driven photocatalytic dye degradation, J. Phys. Chem. Solids 154 (2021), 110075.

[56] S. Zhao, D. Pan, Q. Liang, M. Zhou, C. Yao, S. Xu, Z.Y. Li, Ultrathin NiAl-layered double hydroxides grown on 2D Ti_3C_2Tx MXene to construct core–shell heterostructures for enhanced photocatalytic CO_2 reduction, J. Phys. Chem. C 125 (2021) 10207–10218.

[57] S. Zhao, Q. Liang, W. Gao, M. Zhou, C. Yao, S. Xu, Z.Y. Li, In situ growth of $ZnIn_2S_4$ on MOF-Derived Ni-Fe LDH to construct ternary-shelled nanotubes for efficient photocatalytic hydrogen evolution, Inorg. Chem. 60 (2021) 9762–9772.

[58] Z. Liu, S. Fan, X. Li, Z. Niu, J. Wang, C. Bai, J. Duan, M.O. Tadé, S. Liu, Synergistic effect of single-atom Cu and hierarchical polyhedron-like Ta_3N_5/$CdIn_2S_4$ S-scheme heterojunction for boosting photocatalytic NH_3 synthesis, Appl. Catal. B: Environ. 327 (2023), 122416.

[59] L. Xu, J. Wang, Magnetic nanoscaled Fe_3O_4/CeO_2 composite as an efficient Fenton-like heterogeneous catalyst for degradation of 4-chlorophenol, Environ. Sci. Technol. 46 (2012) 10145–10153.

[60] G. Eshaq, S. Wang, H. Sun, M. Sillanpaa, Superior performance of $FeVO_4$@CeO_2 uniform core-shell nanostructures in heterogeneous Fenton-sonophotocatalytic degradation of 4-nitrophenol, J. Hazard. Mater. 382 (2020), 121059.